Human cochlear hydrodynamics: A high-resolution µCT-based finite element study

Annalisa De Paolis [a], Hirobumi Watanabe [b], Jeremy T. Nelson [c], Marom Bikson [a], Mark Packer [c], Luis Cardoso [a,*]

[a] The Department of Biomedical Engineering, Grove School of Engineering of The City College and The Graduate School of The City University of New York, New York, NY 10031, USA
[b] Department of Mechanical Engineering, Columbia University, 220 Mudd Building 500 West 120th Street, New York, NY 10027, USA
[c] DoD Hearing Center of Excellence, 59MDW/SG02O, 2200 Bergquist Drive, Suite 1 Lackland, AFB, TX 78236, USA

ARTICLE INFO

ABSTRACT

Measurements of perilymph hydrodynamics in the human cochlea are scarce, being mostly limited to the fluid pressure at the basal or apical turn of the scalae vestibuli and tympani. Indeed, measurements of fluid pressure or volumetric flow rate have only been reported in animal models. In this study we imaged the human ear at 6.7 and 3-µm resolution using µCT scanning to produce highly accurate 3D models of the entire ear and particularly the cochlea scalae. We used a contrast agent to better distinguish soft from hard tissues, including the auditory canal, tympanic membrane, malleus, incus, stapes, ligaments, oval and round window, scalae vestibule and tympani. Using a Computational Fluid Dynamics (CFD) approach and this anatomically correct 3D model of the human cochlea, we examined the pressure and perilymph flow velocity as a function of location, time and frequency within the auditory range. Perimeter, surface, hydraulic diameter, Womersley and Reynolds numbers were computed every 45° of rotation around the central axis of the cochlear spiral. CFD results showed both spatial and temporal pressure gradients along the cochlea. Small Reynolds number and large Womersley values indicate that the perilymph fluid flow at auditory frequencies is laminar and its velocity profile is plug-like. The pressure was found 102–106° out of phase with the fluid flow velocity at the scalae vestibule and tympani, respectively. The average flow velocity was found in the sub-µm/s to nm/s range at 20–100 Hz, and below the nm/s range at 1–20 kHz.

© 2016 Elsevier Ltd. All rights reserved.

1. Introduction

In the auditory system, sound propagates down the ear canal producing the vibration of the tympanic membrane and the middle ear ossicles. The oscillation of the stapes against the oval window membrane (OWM) produces a pressure increase in the cochlear fluid that is relieved by the round window membrane (RWM). This phenomenon results in a pressure difference across the scala media, which is at the origin of the travelling wave (TW) on the BM and of the relative motion of the hair cells in the organ of Corti (OC), responsible for the auditory nerve firing (Von Bekesy, 1960; Siebert, 1974; Voss et al., 1996).

The coupling between the hydrodynamics of the perilymph and the biomechanics of the basilar membrane is essential to explain the generation of the TW and the mechanotransduction process in the organ of Corti. However, difficulties arising from the inaccessibility of the cochlea in vivo have limited the experimental characterization of human cochlea mechanics and fluid dynamics to cadaveric samples, where active processes cannot be recorded (Voldrich, 1978). Olson's (1998, 1999) in vivo pressure measurements in the gerbil showed for the first time the interference of "fast" and "slow" waves in the BM. The measurements were performed with a micro-tip sensor inserted in the ST close to the BM. Nakajima et al., (2009) provided simultaneous sound pressure measurements in the SV and ST of the cochlea in human cadaveric temporal bone, and Kale and Olson (2015) measured the pressure in both SM and ST in the gerbil cochlea in vivo. Kringlebotn (1995) reported measurements of RW volume displacement resulting from driving the stapes in a piston-like manner in a post-mortem human temporal bone, showing that the magnitude of RW volume displacements were only 60–70% of those at the OW. Supporting these reports, Salt et al. (1986) and Ohyama et al. (1988) quantified the rate of perilymph flow via the movement of a tracer
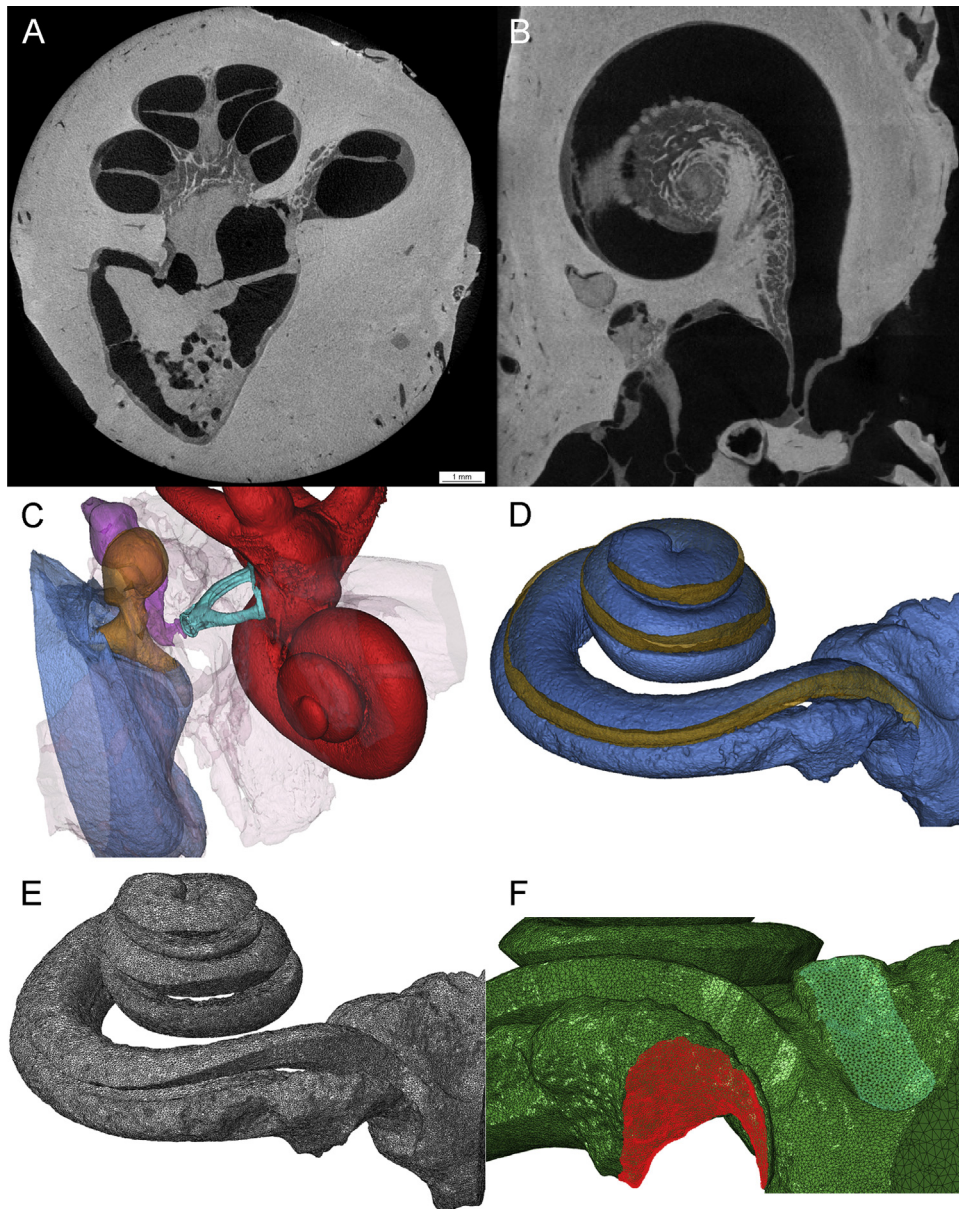
Fig. 1. High resolution images (1A–B) and 3D reconstruction of the human ear (1C). Most ear structures can be clearly defines (1C), including the tympanum (blue), incus (fucsia), malleus (brown), stapes (cyan), cochlea (red), soft tissues and auditory nerve (light pink). (1D) Three-dimensional reconstructions of the scalae vestibuli and tympani (blue) and scala media (gold). (1E) Finite element mesh (element size < 100 um), oval and round window membrane regions showing the boundary conditions (1F) where the inlet and outlet pressure waveform were applied. (For interpretation of the references to color in this figure legend, the reader is referred to the web version of this article.)

(tri-methyl-phenyl-ammonium, TMPA) using an ion-tracer technique. The fluid flow rate measured in the ST in the apical direction was 1.6 nL/min, and the spread of tracer was dominated by passive diffusion processes with very little contribution from endolymph flow.

Numerous mathematical models have been developed during the past decades towards a better understanding of the inner ear hydrodynamics. Varin and Petrov (2009) and Reichenbach and Hudspeth (2014) provided the mathematical formalism to describe the surface wave that rise at the interface between BM soft tissue and endolymph. The perilymph is generally considered incompressible and the bone infinitely stiff. This assumption is based on the large wavelengths when compared with the cochlear size in the human hearing range. Thus, the amount of fluid displaced at the OWM must equal that at the RWM, but with the opposite phase. To test the validity of this hypothesis, Stenfelt et al. (2004) measured the fluid volume displacement at the RW and the OW

for air conducted (AC) and bone conducted (BC) stimulations in temporal bone specimens using Laser Doppler Vibrometry. Their results proved the validity of the assumption in case of AC sound, but not for BC. Edom et al. (2013) investigated the effect of a piston-like or rocking stapes motion on the cochlear fluid flow and the basilar membrane motion in a 2D box model of the cochlea. Kassemi et al. (2005) reported the endolymphatic velocity and pressure fields on the lateral semicircular canal system of the inner ear. Despite the contribution of these studies in illuminating cochlear mechanics, to our understanding, an anatomically accurate characterization of the perilymph hydrodynamics in the human cochlea is still missing in the literature.

In the present study we introduce a detailed 3D μCT-based human cochlea model of the perilymph in the SV and the ST. The use of CFD analysis enables us to examine the effect of morphology and frequency on the fluid flow inside the SV and ST when a sinusoidal pressure stimulus is applied at the OW and RW. A
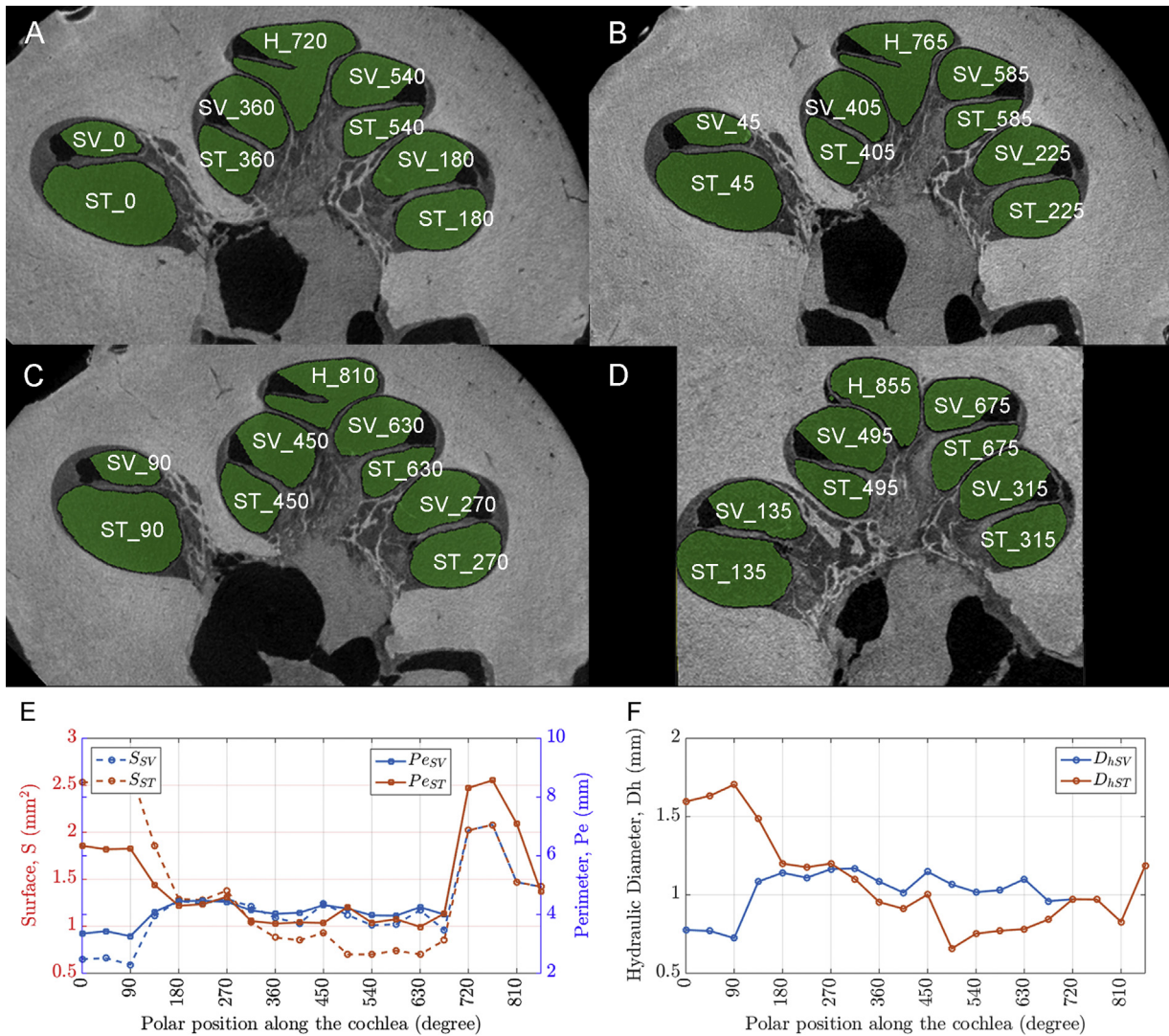
Fig. 2. MicroCT images showing four planes rotated every 45° around the central axis of the cochlea spiral (2A-D). Location of the SV and ST cross surface area on each plane, where the polar position starts in the area closest to the oval window membrane, or base of the cochlea, and increases towards the apex. The cross surface area, S, perimeter, Pe, and Hydraulic diameter, Dh, displayed as a function of their polar position in the human cochlea (2E-F).

characterization of the fluid pattern including the Womersley (Wo) and Reynolds (Re) numbers is also provided.

2. Material and methods

Two temporal bones (female, 62 yr old) were explanted right after death and placed in dry ice until arrival to our laboratory, where they were fixed in 10% buffered formaldehyde for more than 1 week. The temporal bones were rinsed in water during 15 min and a cylindrical region of interest, including the auditory canal, middle and inner ear was cut using a 25 mm diameter, low-speed hollow saw under continuous irrigation. Trabecular bone surrounding the cochlea was trimmed away using a spherical bit of 1 mm in diameter and an opening was produced in the semicircular canals and in the cochlea wall, next to the round window to remove the perilymph.

The right ear was imaged using a high-resolution micro computed tomography (HR-μCT) system (1172, SkyScan, Belgium). Scanning was performed at 100 kV and 100 μA, using a 0.5 mm thick aluminum filter to reduce beam hardening artifacts, and acquiring 5 frames per X-ray angular projection to increase the signal to noise ratio of images. Images of the ear canal, middle and inner ear were acquired at 6.7-μm resolution using 1767 ms integration time per frame and 683 angular projections.

The left ear was stained with a contrast agent to increase the X-ray absorption by soft tissue and enhance its image contrast under HR-μCT. We used 400 ml of Iodine Potasium Iodide, IKI, 5% (wt/v) iodine (I_2) and 10% (wt/v) potassium iodide (KI) mixed in distilled water (0.1 Normal/0.05 M, Fisher Scientific, USA). A pump was used to circulate IKI inside the scalae vestibuli and tympani to facilitate the diffusion of IKI into the soft tissues in the cochlea. After 24 h of incubation, the IKI was removed from the inner ear and μCT-scanned at 3-μm using a similar protocol

to the one used for the right ear. A standard reconstruction algorithm (Feldkamp cone beam) was used to generate images using NRecon software (V1.6.1.2, SkyScan, Belgium). Images were compensated during the reconstruction process for thermal shifting of the X-ray source, misalignment of the rotation axis, ring artifacts and beam hardening (Gu et al., 2012; Souzanchi et al., 2012; Palacio-Mancheno et al., 2014). The whole ear scan comprised more than 7100 cross-section reconstructed images.

The stack of HR-μCT images from the right ear sample was used to create a three dimensional reconstruction of the auditory canal, middle and inner ear. Images were binned with a factor 5 to be imported in Mimics Research (version 19, Materialise, Leuven, Belgium), and the regions corresponding to air, soft, and calcified tissue within the ear were segmented apart based on its mass density (i.e. different gray color level proportional to its X-ray absorption) using an automated thresholding algorithm. Masks representing the 3D volume of tympanus, incus, malleus, stapes, cochlea, soft tissues, and auditory nerve were created. HR-μCT images from the left ear sample were used to create a 3D reconstruction of the scalae vestibuli, tympani and media in the cochlea. Since the Reissner's membrane is not easily observed, the separation between the scala vestibuli and scala media was segmented based on the location of the tectorial membrane and the morphology of the scalae vestibuli on each image.

2.1. Computational fluid dynamic simulation

The transient and steady state fluid dynamic behavior of the perilymph inside the SV and ST of the left human ear was investigated in Abaqus/CFD (V. 6.14 Simulia, Providence, RI) using an explicit time-marching integration approach. The 3D mask of the perilymph was transferred from Mimics into 3Matic Research (version 11,
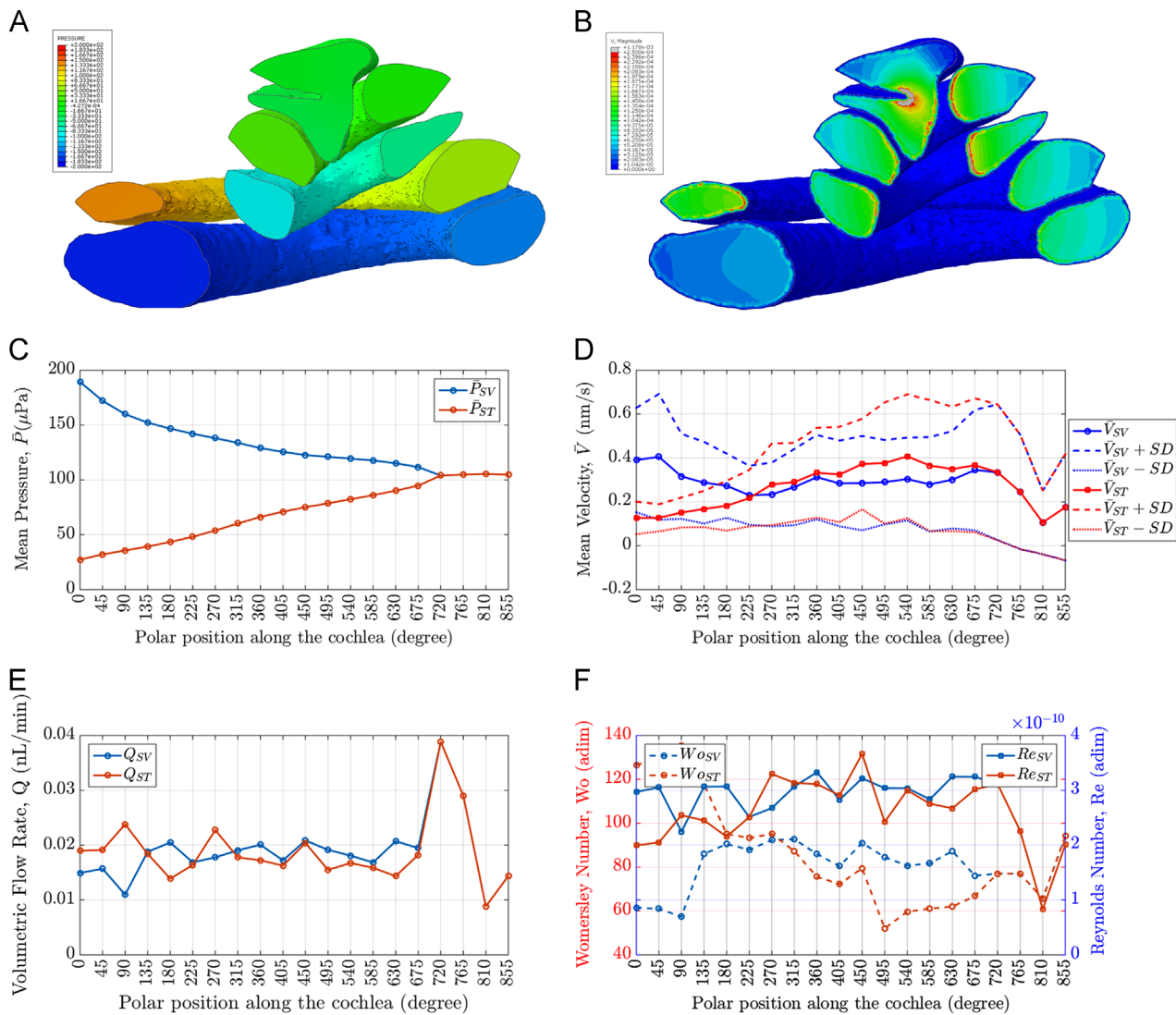
Fig. 3. Mean pressure, *P*, velocity, *V* (3A-B), volumetric flow rate, *Q*, Womersley number, Wo, and Reynolds number, Re, reported as a function of the polar position along the human cochlea in both the SV and ST. The pressure difference between SV and ST is higher at the base of the cochlea and becomes the same pressure at the apex (3C). The flow velocity in both scalae is similar, and statistically not significantly different along the polar position of the cochlea (3D). The volumetric flow rate at the SV and ST is similar in most of the analyzed locations in the cochlea, but increases close to the helicothema (3E). The Womersley and Reynolds numbers vary slightly with location within the cochlea, both indicating that the flow is laminar and plug-like (3F).

Materialise, Leuven, Belgium) for the generation of a 3D volumetric mesh. The finite element mesh was then exported from 3Matic into Abaqus, where the CFD problem was solved. The perilymph was assumed to be Newtonian, incompressible and viscous with a volumetric mass density of $\rho = 1E+3 \text{ kg/m}^3$, and dynamic viscosity of $\mu = 1E\text{-}3 \text{ Pa s}$ (Gan et al., 2007). The fluid flow behavior is governed by the Navier-Stokes equations for an incompressible, viscous fluid where **g** is the acceleration of gravity and **v** and *P* are respectively the flow velocity and the pressure,

$$\rho\left(\frac{\partial \mathbf{v}}{\partial t} + \mathbf{v} \cdot \nabla \mathbf{v}\right) = -\nabla P + \mu \nabla^2 \mathbf{v} + \rho \mathbf{g} \tag{1}$$

and the continuity equation for incompressible flows

$$\frac{\partial \rho}{\partial t} + \nabla \cdot (\rho \mathbf{v}) = 0, \quad \nabla \cdot \mathbf{v} = 0 \tag{2}$$

CFD simulations were conducted using physiological pressure conditions applied to the oval and round window membranes according to the data reported by Nakajima et al. (2009) at 1 kHz for a 20 dB SPL stimulation. A pure tone was used to stimulate the fluid domain inlet (oval window membrane) and outlet (round window membrane) with a 2E-4 Pa and 2.5E-5 Pa peak magnitude pressure, respectively. The outer boundary of the SV and ST was considered to be perfectly rigid, with no slip, and no penetration boundary wall conditions. The frequencies investigated were 20 Hz, 100 Hz, 1 kHz, 5 kHz, 10 kHz or 20 kHz, and the time step increment, Δt, was selected as 1/20 of the time period, *T*, for each frequency considered. The time integration parameter in Abaqus was set by default to $\theta = 0.5$, producing a second order accurate semi-implicit method suitable for time-accurate

transient analysis. The total simulation time was 200 ms in order to capture both transient and steady state response in all simulations.

2.2. Convergence test

A mesh convergence analysis for the finite element size was performed using element sizes of 100, 150, 200, 250 and 500 µm, resulting in models with 3.2 million, 908,507, 375,159, 187,266 and 21,237 tetrahedral fluid elements (FC3D4). The 100 µm-mesh size model resulted in an element size to wavelength ratio, 100 µm/75 mm = 0.00133 for the highest frequency. However, such small element size is necessary to well depict the morphology of the SV and ST. The coarser meshes lead to percentage errors on the mean velocity at the basal turn of the model of 4.11%, 10.56%, 19.39% and 34.58% respectively when compared with the 100 µm-mesh size model. For these reasons, the 100 µm-mesh size was selected as the most accurate to capture the expected variations in pressure and velocity. CFD simulations were performed on a high-end workstation with 24 core Xeon CPUs @ 2.7 GHz, graphic accelerator with 2700 GPU cores and 12 GB, and 512 GB of RAM. The CPU time for each simulation varied between 1 h–36 h per simulation for the finest mesh at 20 Hz and 20 kHz, respectively.

3. Results

The HR-µCT images from the right ear sample showed excellent contrast between calcified, soft tissues and air. Fig. 1A-B shows
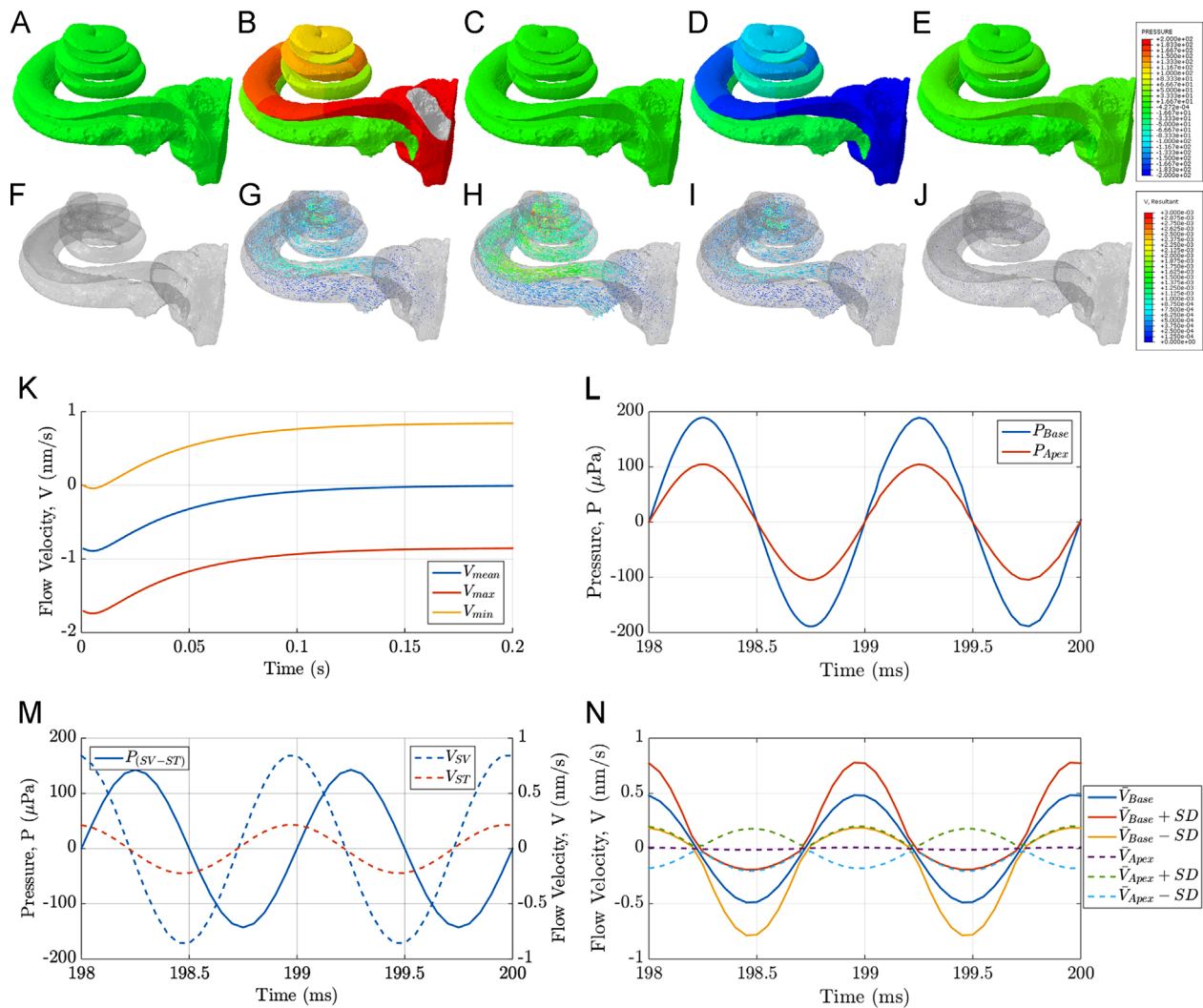
Fig. 4. Hydrodynamics of the human cochlea as a function of time. Perilymph pressure at different time points (0%, 25%, 50%, 75% and 100% of a cycle) within the cochlea for a 1 kHz sinusoidal pressure waveform (4A-E). Corresponding fluid velocity vector field at the same time points (4F-J). Profiles of the mean, max and min flow velocity, v, in the scala vestibuli in the transient ($t < 0.15$ s) and stable state ($t \geq 0.15$ s) for 1 kHz (4K). Plot of the 1 kHz sinusoidal pressure waveform at the base and apex of the cochlea in the last two milliseconds of the stable state (4L). Comparison between the differential pressure between scala vestibule and scala tympani and the flow velocity computed for two points at the center of the scalae at 0° location for the same time interval showing the time delay and the fluid flow mean velocity, upper and lower variance at the base and the apex for the (4N). (For interpretation of the references to color in this figure legend, the reader is referred to the web version of this article.)

cross and axial sections of the cochlea, where the SV and ST are clearly defined. The auditory nerve, spiral ligament, oval and round window membranes, as well as basilar and tectorial membranes were clearly visible in the scans. On the contrary, the Reissner's membrane was not always clearly observable. Thus, the boundary between SM and SV was determined based on the location of the tectorial membrane and the stria vascularis. Fig. 1C is a 3D reconstruction of the right ear from HR-µCT displaying the tympanic membrane (blue), malleus (brown), incus (fuchsia), stapes (cyan), cochlea (red), soft tissues and auditory nerve (light pink). In Fig. 1D, a 3D reconstruction of the scalae vestibuli and tympani (blue color) and scala media (gold color) is shown. The finite element mesh (element size < 100 µm) of the 3D volume representing of the SV and ST is shown in Fig. 1E, and the regions corresponding to the oval and round window membranes, selected respectively as the inlet and the outlet of the model, are displayed in light green and red color in Fig. 1F.

In order to investigate the variation in the inner ear hydrodynamics as a function of the anatomical location within the human cochlea, the cochlear spiral was sectioned with planes at 0°, 45°, 90° and 135° around the central axis of the spiral. Fig. 2A–D

shows HR-µCT images of the cutting planes and the corresponding sections of the SV and the ST. The surface area, S, and perimeter, Pe, were measured on each of those sections, and reported as a function of their polar location, from base to apex, in Fig. 2E. For each polar location, the surface area of the SV and ST is almost constant along the cochlear spiral, with the only exception of the basal turn and the helicotrema, where the SV slightly increases in size while the ST size decreases. The same trend can be observed for the perimeter of both scalae, even though in this case the increase at the helicotrema is four times the corresponding increase in the surface. The surface and perimeter values reported in Fig. 2E were then used to calculate the hydraulic diameter of the cochlea in each section (Fig. 2F). The total volume of the perilymph was $V_t \simeq 93$ mm^3 = 93 µL.

The distribution of the pressure, mean perilymph velocity, and volumetric flow rate along the SV and ST for a 1 kHz tone pressure wave is reported in Fig. 3. Fig. 3A-B displays the distribution of the pressure and flow velocity at various locations within the human cochlea spiral at the time of peak pressure within the steady state response. The highest velocity appears close to the helicotrema. Fig. 3C shows the pressure in the SV and ST, where the 0° location
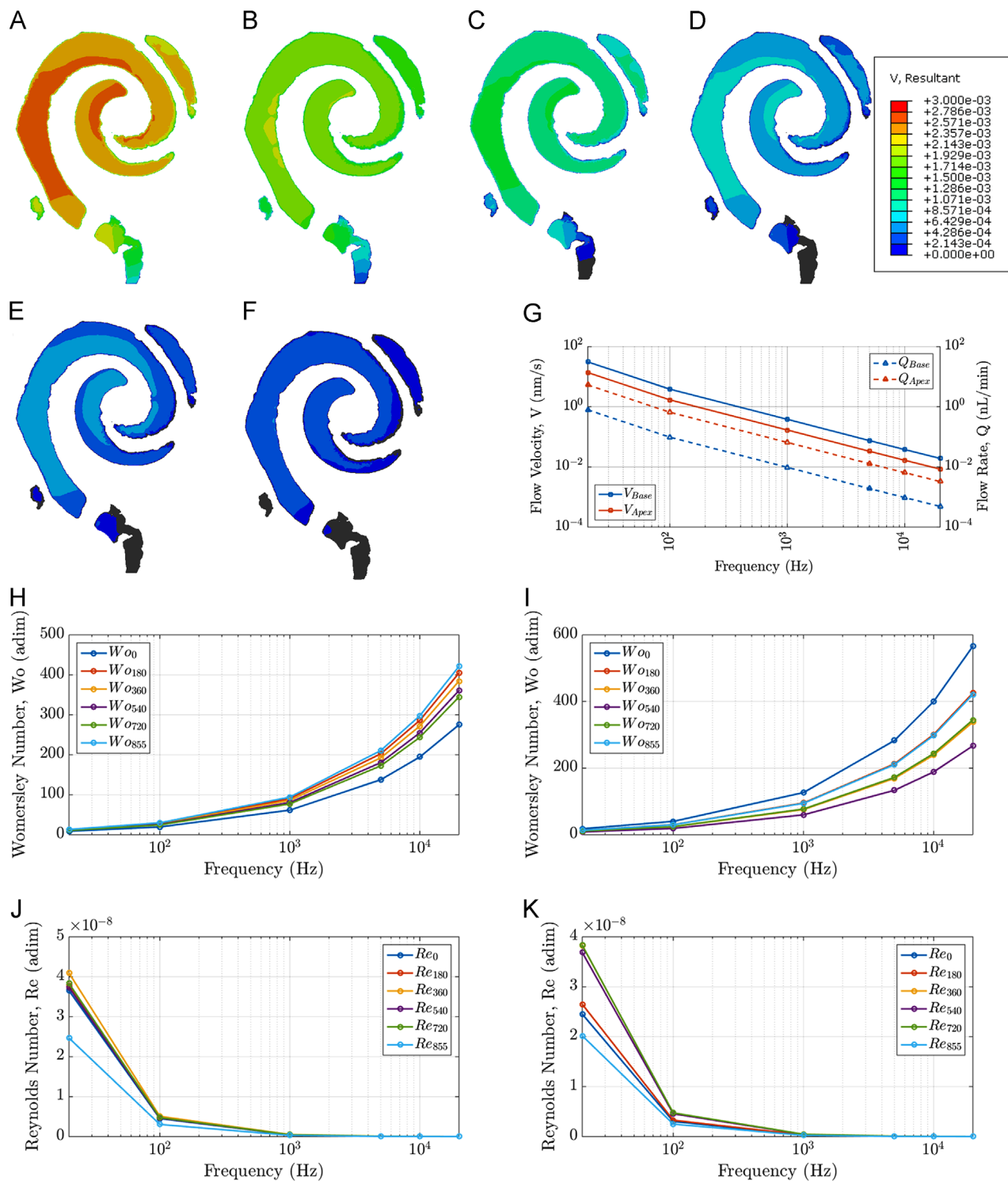
Fig. 5. Hydrodynamics of the human cochlea as a function of frequency. Representative cross section plots of the flow velocity distribution at different locations of the cochlea with increasing frequency (5A-F). Flow velocity, v and flow rate, Q, as a function of frequency at the base and apex of the cochlea, (5G). Womersley (H-I) and Reynolds number (J-K) as a function of frequency at the base and apex of the human cochlea. Womersley and Reynolds numbers support the development of a laminar and plug-like flow.

has a pressure close to the pressure applied at the OWM and RWM, respectively. The pressure decreases along the SV and increases in the ST. At the helicotrema, 720° to 855° angle location, the pressure equalizes. The difference in mean velocity along the cochlea between the two scalae is not significant (Fig. 3H). However, the increasing standard deviation along the cochlea is an

index of the presence of more dispersed values for the velocity at the apex when compared with the base. The volumetric flow rate is similar in both SV and ST along most of the cochlea length, and increases significantly at the helicotrema accordingly to the increase in surface area by the junction of the two scalae (Fig. 3E). Data obtained from the anatomical measurements of surface and

perimeter (Fig. 2E) were used to compute Reynolds and Womersley numbers for all the polar locations considered in the study. In Fig. 3F the results for a stimulation of 1 kHz at the peak of the sinusoid are reported.

The variation of pressure and flow velocity as a function of time is reported in Fig. 4 for the transient and the final two cycles of the steady state response at 1 kHz. Fig. 4A-E displays the pressure map within the cochlea at 0%, 25%, 50%, 75% and 100% of a sinusoidal cycle. For these plots, the pressure at the RWM is held as reference in green color, and the pressure at the OWM changes from a maximum in red color to a minimum in blue color. The changes in flow velocity associated with the time varying pressure are shown in Fig. 4F-J at the same time points as Fig. 4A-E. The flow stream increases to a maximum in Fig. 4H and decreases to a value close to zero at the end of the cycle. Fig. 4K shows the transient behavior of the mean, max and min fluid flow velocity for the whole 200 ms simulation time. It is clearly observed that the transient response lasts 150 ms approximately, and the perilymph dynamics has reached its steady state within the 150–200 ms time period. Fig. 4L displays the last two cycles of the 1 kHz pressure waveform at the base and apex, demonstrating the pressure waveforms are in phase and have different magnitude. The phase delay between the pressure and fluid velocity was quantified at the SV and ST for all tested velocities once the system reached steady state. It was found that the perilymph velocity at the base of the SV had a constant lag phase equal to 102.64°, and a lag phase of 106.61° at the base of the ST (Fig. 4M). In Fig. 4N, the mean, upper and lower variance of the flow velocity at the base and apex are shown, in which the range of velocities span from zero at the wall to a maximum close to the center of each section. It should be noted, however, that the profile of flow velocities at each section is not evenly distributed, having higher velocities close to the inner wall.

Representative cross section plots of the flow velocity distribution at a given z-level plane of the cochlea for all tested frequencies showing isosurfaces in log scaled color in Fig. 5A-F. The variation of flow velocity and volumetric flow rate at the base and the apex of the cochlea are reported versus frequency in Fig. 5G. The flow velocity and flow rate data shows a monotonic decrease in velocity as the frequency of the stimulus increases. The volumetric flow rates vary by four orders of magnitude, from nL/min at 20 Hz to pL/min rates at 20 kHz (Fig. 5G). Womersley number at the base (Fig. 5H) and apex (Fig. 5I), as well as the Reynolds number at the base (Fig. 5J) and apex (Fig. 5K) are shown as a function of frequency. Womersley number varies from 8.12 to $6.04E+2$ for the range of frequencies analyzed, while the Reynolds number decreases by several orders of magnitude, between $O(E-8)$ and $O(E-12)$ as the frequency of the stimulus increases.

4. Discussion

The 3D hydrodynamics of the perilymph pressure and velocity patterns were investigated as a function of anatomical location, time and frequency, using the Navier-Stokes equations for incompressible viscous fluid in anatomically accurate models of the human ear. We combined for the first time high-resolution μCT imaging with CFD simulations to investigate the fluid dynamics of the perilymph contained in the scalae vestibuli and tympani of a human cochlea. HR-μCT images provide exquisite detail of the anatomy of both soft and hard tissues in the human ear.

Our results show that the perilymph flow velocity does not change much from base to apex, being just slightly different when comparing SV and ST at the base of the cochlea. Interestingly, the maximum of the velocity is always close to the internal face of the cochlear ducts suggesting a possible role of the coiling which is neglected by most of the models of the cochlea, as

pointed by Manoussaki and Chadwick (2000). In turn, the fluid flow velocity has four orders of magnitude variation (from sub-μm/s to sub-nm/s) as a function of frequency within the auditory range (Fig. 5). While such small perilymph velocities seem unlikely to contribute significantly to the stimulation of the organ of Corti, the numerical results confirm the presence of local and temporal pressure gradients between scala vestibuli and scala tympani, which depends on the hydraulic diameter of both scalae at the location along the cochlea. This significant pressure gradient is most likely the driving force responsible for the temporal displacements occurring in the scala media and the stimulation of the organ of Corti. The pressure between scalae vestibuli and tympani is equalized at the helicotrema, where on the contrary of what is presented in traditional straight cochlear models with regular cross section shape (Gan et al., 2007; Kim et al., 2011, Kwacz et al., 2013) we found an increase of the section of the cochlear duct which lead to a decrease of the mean fluid velocity and an increase of the volumetric flow rate.

Similarly to the fluid velocity, the volumetric flow rate determined in our model greatly varies as a function of the frequency. The predicted volumetric flow rate at low frequencies is in the nL/min range, similar to the diffusion-based volumetric flow rate reported by Ohyama et al. (1988) in guinea pig (1.6 nL/min). Thus, very low frequency stimulus could possibly increase the transport of therapeutic drugs in the cochlea (Watanabe et al., 2016). Also, the very small Reynolds numbers found in all our results indicate that the flow is laminar, and the large Womersley numbers confirms that the flow profile is plug-like, with a boundary layer extremely thin and practically negligible (Lesser and Berkley, 1972). The plug-like flow also explains the phase delay between pressure and flow velocity inside the two scalae.

The current study has some limitations. Energy dissipation phenomena were not considered because the soft tissue was omitted from the CFD analyses. Therefore, a study of the interaction between perilymph and cochlear partition mechanics in a HR-μCT based model of the human cochlea is needed, and it will be investigated in a future study. Also, we were not able to fully resolve the Reissner's membrane delimitating the scala vestibuli from the scala media along the entire path of the cochlear spiral. Further efforts are necessary to reliably image the Reissner membrane using μCT. Nevertheless, this study is the first to investigate the hydrodynamic behavior of the perilymph inside the human cochlea, based on accurate anatomy obtained from HR-μCT images, whereas most cochlea modeling has been limited to animal, mathematical and numerical models with simplified morphology of the scalae vestibuli and tympani. The results of the numerical simulations in our study provide perilymph velocities in the order of ~100 nm/s at 20 Hz, 0.4 nm/s at 1 kHz and 0.01 nm/s at 20 kHz. Such small flow velocity is a consequence of a very small (acoustic level) pressure difference across the scalae vestibule and tympani, in the order of 200 μPa. Unfortunately, there is a lack of experimental measurements of the perilymph velocity in the literature, and such predicted velocities will need to be validated as measurements of the perilymph velocity become available in the field.

Conflict of interest

The authors have no conflict of interest.

Acknowledgements

References

Edom, E., Obrist, D., Henniger, R, Kleiser, L., 2013. The effect of rocking stapes motion on the cochlear fluid flow and the basilar membrane motion. J. Acoust. Soc. Am. 134 (5), 3749–3758.

Kale, S.S., Olson, E.S., 2015. Intracochlear scala media pressure measurement: implications for models of cochlear mechanics. Biophys. J. 109, 2678–2688.

Gan, R.Z., Reeves, B.P., Wang, X., 2007. Modeling sound transmission from ear canal to cochlea. Ann. Biomed. Eng 35 (12), 2180–2195.

Gu, X.I., Palacio-Mancheno, P.E., Leong, D.J., Borisov, Y.A., Williams, E., Maldonado, N., Laudier, D., Majeska, R.J., Schaffler, M.B., Sun, H.B., Cardoso, L., 2012. High resolution micro arthrography of hard and soft tissues in a murine model. Osteoarthr. Cartil 10 (9), 1011–1019.

Kassemi, M., Deserranno, D., Oas, J.G., 2005. Fluid–structural interactions inner ear. Comput. Struct. 83, 181–189.

Kim, N., Homma, K., Puria, S., 2011. Inertial bone conduction: symmetric and anti-symmetric components. J. Assoc. Res. Otolaryngol. 12 (3), 261–279.

Kringlebotn, M., 1995. The equality of volume displacements in the inner ear windows. J. Acoust. Soc. Am. 98, 192–196.

Kwacz, M., Marek, P., Borkowski, P., Mrowka, M., 2013. A three-dimensional finite element model of round window membrane vibration before and after stape-dotomy surgery. Biomech. Model. Mechanobiol12 (6), 1243–1261.

Lesser, M.B., Berkley, D.A., 1972. Fluid mechanics of the cochlea. J. Fluid Mech. 51, 497–512.

Manoussaki, D., Chadwick, R.S., 2000. Effects of geometry on fluid loading in a coiled cochlea. SIAM J. Appl. Math. 61, 369–386.

Nakajima, H.H., Dong, W., Olson, E.S., Merchant, S.N., Ravicz, M.E., Rosowski, J.J., 2009. Differential intracochlear sound pressure measurements in normal human temporal bones. J. Assoc. Res. Otolaryngol.: JARO 10, 23–36.

Ohyama, K., Salt, A.N., Thalmann, R., 1988. Volume flow rate of perilymph in the guinea-pig cochlea. Hear. Res. 35, 119–129.

Olson, E., 1998. Observing middle ear and inner ear mechanics with novel intra-cochlear pressure sensor. J. Acoust. Soc. Am. (6), 3445–3463.

Olson, E., 1999. Direct measurement of intra-cochlear pressure waves. Nature 402, 526–529.

Palacio-Mancheno, P.E., Larriera, A.I., Cardoso, L., Fritton, S.P., 2014. 3D assessment of cortical bone porosity and tissue mineral density using high-resolution micro-CT: effects of resolution and threshold method. J. Bone Miner. Res. 29 (1), 142–150.

Reichenbach, T., Hudspeth, A.J., 2014. The physics of hearing: fluid mechanics and the active process of the inner ear. Reports on Progress in Physics. Physical Society (Great Britain) 77, 0, 7, 6601, -4885/77/7/076601. Epub 2014 Jul 9.

Salt, A.N., Thalmann, R., Marcus, D.C., Bohne, B.A., 1986. Direct measurement of longitudinal endolymph flow rate in the guinea pig cochlea. Hear. Res. 23, 141–151.

Siebert, W.M., 1974. Ranke revisited-—a simple short-wave cochlear model. J. Acoust. Soc. Am. 56, 594–600.

Souzanchi, M.F., Palacio-Mancheno, P., Borisov, Y.A., Cardoso, L., Cowin, S.C., 2012. Microarchitecture and bone quality in the human calcaneus: local variations of fabric anisotropy. J. Bone Miner. Res. 27 (12), 2562–2572 (PMCID: 3500573).

Stenfelt, S., Hato, N., Goode, R.L., 2004. Fluid volume displacement at the oval and round windows with air and bone conduction stimulation. J. Acoust. Soc. Am. 115, 797–812.

Varin, V.P., Petrov, Alexander G., 2009. A hydrodynamic model of human cochlea. Comput. Math. Math. Phys. 49 (9), 16321647.

Voldrich, L., 1978. Mechanical properties of basilar membrane. Acta Oto-Laryngol. 86, 331–335.

Von Bekesy, G., 1960. Experiments in Hearing. McGrow-Hill, New York.

Voss, S.E., Rosowski, J.J., Peake, W.T., 1996. Is the pressure difference between the oval and round windows the effective acoustic stimulus for the cochlea? J. Acoust. Soc. Am. 100, 1602–1616.

Watanabe, H., Cardoso, L., Lalwani, A.K., Kysar, J.W., 2016. A dual wedge micro-needle for sampling of perilymph solution via round window membrane. Biomed. Microdevices 18 (2), 1–8.